ez et al., ibid. **96**, 4188 (1992).
32. H. R. Gerberich and W. D. Walters, J. Am. Chem. Soc. **83**, 4884 (1961).
33. See (2), (5), and J. A. Berson, L. D. Pedersen, B. K. Carpenter, ibid. **98**, 122 (1976).
34. B. K. Carpenter, Acc. Chem. Res. **25**, 520 (1992).
35. Supported by a grant from the Air Force Office of Scientific Research and by the National Science Foundation. We are grateful to P. B. Dervan, D. A. Dougherty, M. Okumura, J. D. Roberts, and W. von. E. Doering for the helpful discussions. We thank J. A. Berson and B. K. Carpenter for their helpful suggestions and penetrating questions, C. Doubleday Jr. for his interest in this work and for communicating unpublished results, K. Anderson for the preparation of 2,2,5,5-tetramethylcyclopentanone, and L. Bañares for his help in the preliminary work (bulb studies) in this group. Contribution no. 8970 from the Arthur Amos Noyes Laboratory of Chemical Physics.

26 August 1994; accepted 23 September 1994

Origin of Storm Footprints on the Sea Seen by Synthetic Aperture Radar

David Atlas

Spaceborne synthetic aperture radar can detect storm footprints on the sea. Coastal weather radar from Cape Hatteras provides evidence that the echo-free hole at the footprint core is the result of wave damping by rain. The increased radar cross section of the sea surrounding the echo-free hole results from the divergence of the precipitation-forced downdraft impacting the sea. The footprint boundary is the gust front; its orientation is aligned with the direction of the winds aloft, which are transported down with the downdraft, and its length implies downdraft impact 1 hour earlier at a quasi-stationary impact spot. The steady, localized nature of the storm remains a mystery.

Reynolds (1) made the first attempt to explain the reports made by seafarers that rain calms the sea. He attributed this to the turbulence associated with the shedding of vortex rings by the raindrops. A rather complete history of the variety of studies aimed at explaining the wave damping mechanism is given in (2). Unfortunately, the lack of an accepted model leaves the damping mechanism in doubt. The situation is exacerbated by the absence of well-documented observations such as photographs of the sea before and after rain.

This confusion motivated several investigators (2–4) to conduct experiments in wave tanks in which wave amplitude was measured on either side of a section of artificial rain. Unfortunately, the latter are thought to be deficient in several respects (5). The confusion is compounded by the laboratory tank experiments on the backscatter from a rain-perturbed wavy water surface (6–8). In these experiments, 14- and 35-GHz radars were used at incidence angles of 30° to 40°. In all three, the presence of rain increased the radar cross section (RCS) relative to that with winds alone, thus contradicting the idea of rain damping of the short resonant Bragg waves (9) of order 1 to 2 cm. The increased backscatter or RCS of the disturbed surface at vertical polarization was attributed to the rain-induced ripples or ring waves (7), and it was proposed that one may simply add the RCS due to the ring waves to that due to the winds alone (8). But these experiments are also believed to be faulty in the same senses as those on wave damping (5). Moreover, there were no observations made downstream of the small radar footprint where one would expect turbulence to be more fully developed and damping to have taken effect (5).

Distinguished Visiting Scientist, Laboratory for Atmospheres, Goddard Space Flight Center, Greenbelt, MD 20771, USA. E-mail: datlas@gsfcmail.nasa.gov

Therefore, laboratory experiments on the mixing of rain with near-surface water (10) were used in (5) to deduce the damping rates. Although there were no wind waves, this work used drops of sizes up to 5.5 mm impacting both fresh and salt water at terminal velocity; neither of these conditions prevailed in the earlier work. Because the drops were warm and the receiving bath was cold, a thermocline developed; the rate of increase of the depth of the thermocline is then a measure of the average eddy viscosity (5). This is proportional to the flux of kinetic energy from the rain. However, for unknown reasons the viscosity produced by 5.5-mm drops is almost twice that of drops $\leq$3.6 mm in diameter. The rate of wave damping is then determined with the use of theoretical relations (11, 12). Scaling the kinetic energy flux to a rain rate of 150 mm hour^{-1}, one finds the eddy viscosity to be 0.30 cm^2 s^{-1}. The *e*-folding decay times in a mixed layer of fresh and salt water 10 cm deep are 0.017, 1.05, and 17.9 s for short gravity waves with wavelengths of 2, 10, and 30 cm, respectively. This compares with times of 2.4, 60, and 540 s for the same sequence of wavelengths at a molecular viscosity of 0.01 cm^2 s^{-1}. The decay times increase at lesser rain rates but are still smaller than that attributed to molecular viscosity. It was then postulated (5) that the longer waves would also decay because they would no longer receive energy from the shorter ones (13).

Signatures of storm-induced effects on the sea have been seen by synthetic aperture radar (SAR) on board the SEASAT satellite (14, 15). The primary feature is an echo-free hole (EFH) surrounded by a region of enhanced RCS within a well-defined boundary. The EFH was attributed to the damping of the Bragg waves (~30 cm for SEASAT), thus reducing the surface RCS and causing the EFH. The boundary of the surrounding zone of increased RCS was described as a squall line (14). In a reexamination of the latter observations (5), a directional effect was observed such that the RCS was maximum on the radar-facing boundaries of the footprint and weakest on the tangential boundaries. This is the only direct evidence of the orientation of the short resonant gravity waves and thus of the winds diverging from the downdraft that accompanies the heavier rain. The combination of rain core, collocated downdraft, surface winds diverging from the downdraft impact point, and sharp wind boundary is characteristic of a convective storm. In those cases in which the near-surface divergence is particularly sharp, the phenomenon is known as a microburst (16).

Figure 1 shows the SAR image of an area off the Atlantic coast of the United States taken at 1536 UTC on 18 July 1992 at a wavelength of 5.6 cm from the European Remote Sensing Satellite 1 (ERS-1). The three largest precipitation echoes seen at a wavelength of 10 cm by Weather Surveillance Radar 57 (WSR-57) at Cape Hatteras, North Carolina (dashed curves in Fig. 1), are accompanied by strong modulations in the surface RCS. The close association of the two leaves little doubt that the precipitation or the storm-induced winds at the surface, or both, are responsible for the alterations of the surface RCS.

Note that the EFHs occur either at the southwestern edges of the precipitation echoes or within the region of maximum reflectivity and rain rate. Convective storms formed in subtropical and temperate latitudes of the Northern Hemisphere are initiated at their southernmost ends. The region of maximum storm height, rain rate, and drop sizes are found somewhat north of the southern generating point. As noted above, the maximum flux of rain kinetic energy and the greatest eddy viscosity in the near-surface water accompanies the heaviest rain, and for rain of a particular flux, the eddy viscosity is larger where the rain is composed of drops larger than 3.6 mm. These are the zones in which the surface waves would be most rapidly damped provided that the winds are not strong enough to overwhelm the damping effect.

At the 5.6-cm wavelength and 23° nadir angle of the ERS-1 SAR, the Bragg wavelength of surface waves is 10 cm. This varies slightly across the width of the image. Thus, the EFHs represent the areas in which the 10-cm gravity waves have been damped. Because the longer waves derive their energy from the shorter ones, presumably they too have been damped, although we have no direct evidence for this. Swell generated far from the storms would not be damped.

Within the black EFH of the southernmost radar echo seen from Cape Hatteras, we find a small bright spot about 1 km by 1.5 km in size (Fig. 2). It has been suggested that this is the result of scattering from the splash products of the rain upon impact with the sea surface (5); such products are the crowns, the ring waves, and the stalks or Rayleigh jets (17). However, we have no direct evidence for this explanation of the bright spot. The detection of the splash products depends on the rain intensity and whether or not the splash-producing rain decays or moves off to leave a trail of turbulently mixed water with a smooth surface. Such bright spots appear in about a third of the storm-induced sea echoes seen on the approximately 20 SEASAT and ERS-1 SAR images that I have examined. This implies that the rain responsible for the bright spot has either decayed or moved off, leaving a persistent EFH or wake. There are some still speculative indications of the persistence of the wave damping by the rain for a few tens of minutes (18).

Because the heavier rain and downdraft are generally collocated, one may wonder whether or not the downdraft itself could cause the wave damping. For example, the advancing front of a downdraft such as that found in a microburst is marked by a cone of stagnation in which the horizontal winds are calm. It may then be thought that this is the region in which no short surface gravity waves are generated and where the RCS is so small as to produce the EFH. However, a high-resolution numerical model has shown that the stagnation cone is typically one-third the diameter of the rain shaft (19). The EFHs in Fig. 1 are almost all in the range of 2 to 5 km in diameter, and others (14, 15) measure up to 10 km. Moreover, those in Fig.1 are clearly elongated in the southwest-northeast direction, which, as we shall soon see, is the direction of the winds and the rain. I have also studied the horizontal divergence fields in a series of Doppler radar observations of microbursts (20, 21) and find that the low-level radial wind changes direction by 180° in less than 200 to 300 m (that is, typically 2 to 3 radar pulse widths). If anything, the sharp increase in winds in both directions across this transition zone would cause an increase in RCS. Therefore, it is extremely unlikely that the calm core of the a downdraft such as that in a microburst can explain the reduced RCS and the EFH. We conclude that it is the rain that is responsible for the wave damping and the EFHs.

The pattern of echoes surrounding the EFHs is best formed in the southernmost echo region in Fig. 1. It is composed of a plume-like structure expanding out largely to the northeast with its axis oriented toward 46° (Fig. 2). I have superimposed schematic streamlines to depict the near-surface airflow consistent with the echo pattern. The gust front is most sharply defined on the eastern side because this is where the surface winds are most closely oriented along the illumination direction and where the surface Bragg waves are most nearly aligned with the electromagnetic phase fronts. Also, the left edge of the plume is partially obscured by outflow from the adjacent storm.

It is evident that such a plume could only have been produced by a downdraft impacting at essentially one spot close to the origin of the streamlines in Fig. 2; this is at or near the bright spot and the EFH. It is analogous to a smoke plume flowing from a stationary chimney but inverted (Fig. 3). It also implies that the outflow is virtually steady for the time needed for the plume axis to cover the distance of 36 to 38 km from its source. We show below that the outflow speed is about 10 m s^{-1} and the travel time is therefore about 1 hour. Two questions arise: (i) Why does the axis of the plume point toward the northeast, and (ii)

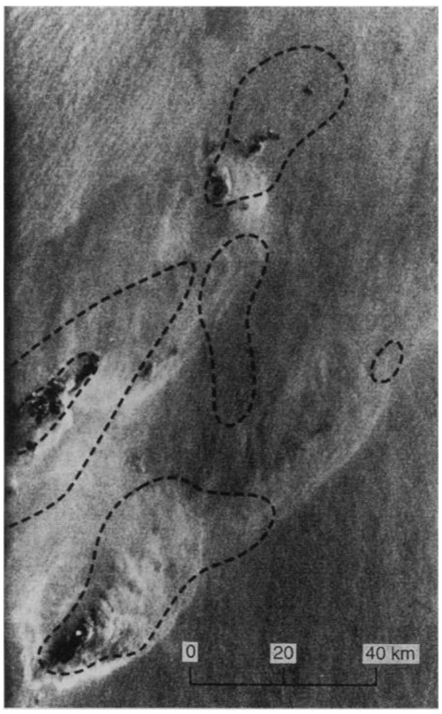

Fig. 1. A 5.6-cm-wavelength ERS-1 SAR image of an area off the Atlantic coast of the United States taken at 1536 UTC on 18 July 1992. Width is 93.3 km; length is 150 km. The vertical boundaries are oriented toward 12° (NNE). The dashed contours are rain reflectivity levels viewed 3 min after the SAR overpass from the 10-cm Cape Hatteras WSR-57 radar. The outer contour represents a reflectivity of 30 dBZ (10 log Z = 30, or Z = 1000 $mm^6\ m^{-3}$; Z is the sum of the sixth power of drop diameter in millimeters per unit volume in cubic meters). The region encompassed by the inner contour corresponds to 30 < 10 log Z < 40 dBZ, or rain rates 2.4 < R < 12 mm $hour^{-1}$ calculated with the nominal relation $Z = 300 R^{1.4}$. The center of the inner contour is 125 km from the Cape Hatteras radar at a bearing of 128°. An expanded view is shown in Fig. 2.

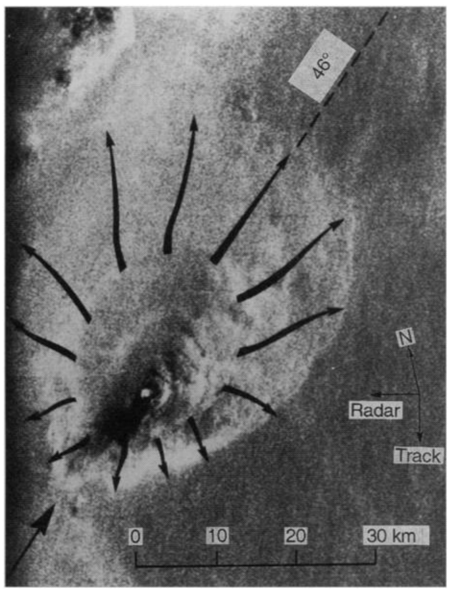

Fig. 2. Expanded view of the plume-like footprint in Fig. 1 showing the satellite track, radar beam, and true north. The tips of the streamlines mark the best estimate of the position of the plume boundary at the overpass time of 1536 UTC. The starting points of the streamlines were terminated to prevent obscuring the sea surface echo structure. The tips of the streamlines mark the outflow boundary that corresponds to the gust front.

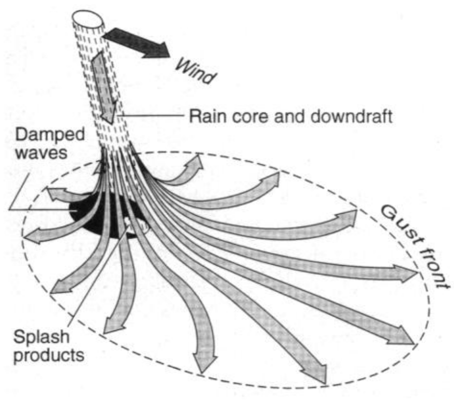

Fig. 3. Schematic of the sea surface footprints and the hypothesized rain and airflow.

how can the source remain fixed and steady for such a long time?

The winds nearest in time and space to the those over the observing area are those observed at Cape Hatteras at 1200 UTC. The surface wind was virtually calm. The winds were southwest ($\pm 10°$) at speeds between 10 and 12 m s^{-1} at all elevations between 1.5 and 6 km; the 0°C level was at 4.5 km. Downdrafts are forced by a combination of precipitation loading, melting, and evaporative chilling and originate close to the melting level (*19*, *22*). The draft transports the horizontal momentum at the generating level down; it is also accelerated by the aforementioned processes but may also be diluted by mixing with the environment. Thus, it is reasonable that the surface outflow winds will come from the southwest, in accord with the plume axis, but its speed could be either more or less than 11 m s^{-1}. Successive radar pictures from the Hatteras radar at 5-min intervals give velocities of 8.6 to 12.3 m s^{-1} from the southwest for the smaller echoes. These are close to the southwest 11-m s^{-1} winds at the generating level. We thus estimate the outflow surface winds as southwest at 10 ± 2 m s^{-1}. This explains the direction of the plume axis and its duration of about 1 hour. Some of the key surface features and the process by which I suggest they arose are shown in Fig. 3.

We have no plausible hypothesis for the observation that the impact zone of the downdraft remains essentially fixed for this period. The Hatteras radar does confirm our deduction that the precipitation echo associated with the plume in Fig. 2 remains fixed in position as it grows in size, whereas the smaller echoes that make up the line extending from the southwest to the northeast move at the speeds noted above. Although it is not uncommon for a topographically or thermally forced thunderstorm over land to remain fixed, no prior observations over the ocean have shown similar behavior. Thus, the localization and steady nature of the downdraft remains a mystery. We can only speculate that this storm was forced by the extremely warm Gulf Stream water (30°C), which was observed the day before by a satellite of the National Oceanic and Atmospheric Administration that was at the position of this storm. Clouds precluded surface temperature measurements on the day of the storm.

Immediately surrounding the bright spot at the northwest end of the EFH, one discerns a bright circular arc. Similar arc-like variations in brightness are also found further outward from the bright spot. Because the surface brightness represents the surface RCS, which varies with the local wind speed, we may assume that the wind varies with distance from the source region. This is a manifestation of the typical fluctuations in updraft and downdraft speeds found in convective storms and the successive waves of the diverging winds from a microburst (*16*). In any case, the fact that one sees the bright spot (that is, the apparent locale of the most intense rain) at observing time also suggests that the heaviest (although hardly intense) rain is still in progress at this time. By the same token, the variations in RCS outward from the bright spot are more recent in origin than is the gust front. In short, the sea surface plume in Fig. 2 provides a fossil footprint of the history of the surface winds in the last hour or so.

We fail to see such a well-formed plume in the other SAR echoes seen in Fig. 1, although one does find boundary lines in the vicinity of each EFH. In those storm areas, one finds a multiplicity of EFHs, indicative of several showers and non–steady-state conditions. Moreover, none of the EFHs contain a bright spot, suggesting that the rain responsible for the EFH is no longer producing the splash products that we have associated with the heavier rain.

In Fig. 1, we also observe that the weather radar echoes are generally larger than their corresponding SAR surface patterns of increased RCS. This is partly because of the large beam width of the Hatteras radar, and also the fact that a substantial portion of the precipitation echoes is composed of light stratiform rainfall with relatively small drops. This and the probable increased winds surrounding the EFH would prevent damping. In short, wave damping does not occur everywhere there is rain, but only where the rain effect exceeds wind wave generation.

One may also inquire as to whether or not the 5.6-cm SAR detects the rain in addition to the short surface gravity waves. A computation with a theoretical relation (*23*) shows that the ERS-1 SAR should detect rain exceeding 20 mm $hour^{-1}$ if the beam is 25% filled and the surface clutter background is zero. However, the Hatteras weather radar fails to show rain rates greater than about 12 mm $hour^{-1}$. Moreover, where the winds exceed a few meters per second, the surface scatter is so large that it would require the integration of an extremely large number of independent pulses to detect the rain in the sea echo (*23*). In other words, the wind-driven sea echoes would obscure even more intense rain. Also, the Hatteras weather radar shows precipitation echo over the EFHs where the surface RCS is negligible; thus, the SAR echoes seen in Figs. 1 and 2 are almost certainly entirely the result of backscatter from the surface.

It is evident that storm-induced variations in the mesoscale winds on the ocean surface will affect the exchange of heat, moisture, and momentum between the air and the sea. Also, the modulation of the surface RCS will introduce micro- to mesoscale errors in wind measurements by radar scatterometry from space. This will be particularly noticeable along squall lines, which generally occur along fronts. Thus, it would be dangerous to attempt to smooth scatterometric winds by eliminating sharp discontinuities and thus obscuring some of the most important features that the method is intended to observe. The storm-forced variations in the RCS of the sea will also produce errors in airborne and spaceborne radar rainfall measurements that are based on algorithms that assume that the storms do not affect the surface RCS. These and other related effects are discussed elsewhere (*5*, *18*).

REFERENCES AND NOTES

1. O. Reynolds, *Proc. Lit. Philos. Soc. Manchester* **14**, 1874 (1875).
2. M. Tsimplis, *J. Phys. Oceanogr.* **22**, 404 (1992).
3. ______ and S. A. Thorpe, *Nature* **342**, 893 (1989).
4. Y. K. Poon, S. Tang, J. Wu, *J. Phys. Oceanogr.* **22**, 976 (1992).
5. D. Atlas, *J. Geophys. Res. C* **99**, 7961 (1994).
6. R. K. Moore *et al.*, *IEEE J. Oceanic Eng.* **4**, 31 (1979).
7. L. F. Bliven, H. Branger, P. Sobieski, J. P. Giovanangeli, *Int. J. Remote Sensing* **14**, 2315 (1993).
8. L. F. Bliven and J. P. Giovanangeli, *ibid.*, p. 855.
9. The Bragg wavelength is the length of a surface wave that equals half of the radar wavelength when projected along the direction of the radar beam. The echoes from the successive peaks of the waves then add constructively.
10. T. Green and D. F. Houk, *J. Fluid Mech.* **90**, 569 (1979).
11. J. A. Nystuen, *J. Geophys. Res. C* **95**, 18353 (1990).
12. Y. L. Yakimov, *Izv. Sib. Otd. Akad. Nauk. SSSR* **5**, 125 (1959).
13. M. S. Longuet-Higgins, *Proc. R. Soc. London Ser. A* **311**, 371 (1969).
14. L. Fu and B. Holt, *Publ. 81–120* (Jet Propulsion Laboratory, Pasedena, CA, 1982).
15. D. B. Ross, *Spaceborne Synthetic Aperture Radar for Oceanography*, R. C. Beal, P. S. DeLeonibus, I. Katz, Eds. (Johns Hopkins Univ. Press, Baltimore, MD, 1981), pp. 75–84.
16. T. T. Fujita and J. McCarthy, *Radar in Meteorology*, D. Atlas, Ed. (American Meteorological Society, Boston, MA, 1990), pp. 657–681.
17. L. B. Wetzel, *Radio Sci.* **25**, 1183 (1990).
18. D. Atlas and P. G. Black, *Bull. Am. Meteorol. Soc.* **75**, 1183 (1994).
19. F. H. Proctor, *J. Atmos. Sci.* **45**, 3137 (1988).
20. M. E. Weber and T. A. Noyes, *Lincoln Lab. J.* **2** (no. 3), 511 (1988).
21. T. A. Noyes, *Proj. Rep. ATC-172* (Lincoln Laboratory, Massachusetts Institute of Technology, Cambridge, MA 1990).
22. F. H. Proctor, *J. Atmos. Sci.* **46**, 2143 (1989).
23. A. Ahamad and R. K. Moore, *Tech. Rep. 8370–3* (Radar Systems and Remote Sensing Laboratory, University of Kansas, Lawrence, KS, 1994).

24. I am indebted to the European Space Agency and to R. Gasporovich for furnishing the SAR imagery, and to J. Marshall Shepherd, A. Negri, and L. Long for assistance. This work was supported by the National Aeronautics and Space Administration under contract NASA 5–32344.

4 May 1994; accepted 15 September 1994